Front. Phys., 2014, 9(5): 598–612
DOI 10.1007/s11467-013-0377-x

REVIEW ARTICLE

# Spin–orbit coupling in Bose–Einstein condensate and degenerate Fermi gases

**Peng-Jun Wang, Jing Zhang**†

*State Key Laboratory of Quantum Optics and Quantum Optics Devices, Institute of Opto-Electronics, Shanxi University, Taiyuan 030006, China*

*Corresponding author. E-mail:* †*jzhang74@sxu.edu.cn, jzhang74@aliyun.com*

*Received July 27, 2013; accepted September 10, 2013*

We review our recent experimental realization and investigation of a spin–orbit (SO) coupled Bose–Einstein condensate (BEC) and quantum degenerate Fermi gas. By using two counter-propagating Raman lasers and controlling the different frequency of two Raman lasers to engineer the atom–light interaction, we first study the SO coupling in BEC. Then we study SO coupling in Fermi gas. We observe the spin dephasing in spin dynamics and momentum distribution asymmetry of the equilibrium state as hallmarks of SO coupling in a Fermi gas. To clearly reveal the property of SO coupling Fermi gas, we also study the momentum-resolved radio-frequency spectroscopy which characterizes the energy–momentum dispersion and spin composition of the quantum states. We observe the change of fermion surfaces in different helicity branches with different atomic density, which indicates that a Lifshitz transition of the Fermi surface topology change can be found by further cooling the system. At last, we study the momentum-resolved Raman spectroscopy of an ultracold Fermi gas.

**Keywords** spin–orbit coupling, Bose–Einstein condensate, Fermi gases, topological change, momentum-resolved radio-frequency spectroscopy, momentum-resolved Raman spectroscopy

**PACS numbers** 67.85.d, 05.30.Fk, 03.75.b, 03.75.Mn

Contents



## 1 Introduction

Quantum degenerate gases are extremely versatile and can be controlled with great precision and high degree, which offer us new opportunities to efficiently simulate quantum condensed matter systems in the extreme physical parameter regimes and gain a deeper understanding of the reality [1–3]. These gases constitute remarkably flexible playgrounds, which can be formed of bosons, fermions, or mixtures of both. Their external environment can be controlled using the potential created by laser light, with harmonic, periodic, quasi-periodic or disordered energy landscapes, such as using optical lattice to control the energy landscape at the single-particle level to simulate quantum phase transitions from a superfluid to a Mott insulator [4], observe Anderson localization in three dimensional disordered potential induced by laser speckle [5]. The particle interaction can be adjusted using Feshbach resonance, such as the controlled collapse of a BEC [6], the formation of ultracold diatomic molecules [7], the realization of the BCS–BEC crossover in dilute gases [8], and the observation of the Efimov spectrum in ultracold gases [9]. However, the only missing ingredient in quantum simulation with quantum degenerate atomic gases is the equivalent of orbital magnetism, which would allow one to mimic the effects of

magnetic or electric fields on the electron's charge, such as quantum Hall effect, spin–orbit (SO) coupling.

SO coupling is an essential phenomenon in condensed matter physics, and exists in all metals, is crucial for the quantum spin hall state and topological insulators. But it is also very weak, only a few of them turn out to be topological insulators. In 2006, a general mechanism for finding topological insulators was proposed and based on band inversion [10], in which the usual ordering of the conduction band and valence band is inverted by SO coupling. Recently, a group increased the SO coupling strength and observed the quantum spin hall effect in HgTe quantum wells grown by molecular-beam epitaxy [11].

A well-known method to imitate magnetic fields in a cloud of electrically neutral atoms is to rotate the gas [12–15], where the transformation to the rotating frame corresponds to giving the particles a fictitious charge, and applying an effective uniform magnetic field. In the experiments with this method, quantized vortices have been observed, which is the hallmark of superfluids or superconductors in a magnetic field [16, 17]. However, because of the limit of rotating frequency and temperature, the effective uniform magnetic field is not strong enough to study quantum Hall physics.

NIST group firstly engineered a new kind of quantum simulator as shown in Refs. [18–21], in which they created experimentally an artificial coupling between the spin of atoms and their center-of-mass motion. To achieve the coupling, they used a pair of lasers to transfer light momentum to the atoms' center-of-mass and create mixed atomic spin states, which are composed of two different spin orientations. The mixed-spin states couple directly with the momentum transferred to the atoms' center-of-mass (orbital) motion, creating a "dressed state", thus leading to an artificial SO coupling. They also studied the low-temperature phases of these interacting SO coupled bosons and observed a quantum phase transition from spatially mixed to spatially separated. The effective vector gauge potential for BEC of $^{87}$Rb by using two crossed 1064 nm optical dipole trap lasers as the Raman beams was studied in our group [22] and later SO coupling in BECs also was realized experimentally by two other groups [23, 24].

In real materials, SO coupling refers to the interaction between the spin and motion degrees of freedom of an electron, which plays an important role in many physical systems over a wide range of energy scales, from determining the electron structure inside an atom to giving birth to topological insulators in solid state materials [25, 26]. All these systems are fermionic, from the viewpoint of quantum simulation it is desirable to experimentally realize SO coupled degenerate Fermi gases, so the SO coupling in Fermi gases holds even more promise. Recently our group firstly observed the SO coupling in an atomic Fermi gas $^{40}$K in which lasers induce strong SO coupling [27], and a team in MIT describes the observation of SO coupling in an atomic Fermi gas $^{6}$Li and a direct spectroscopic measurement of the SO coupled dispersion relation [28].It is should emphasized that all experiments on spin–orbit coupling discussed here utilize Raman laser beams. Due to the Pauli exclusion principle, fermions occupy a large number of momentum states, and are therefore sensitive to global (topological) features of the band structure. Conversely, BEC typically occurs in one or two single-particle states. SO coupled fermionic gases would thus provide ways to explore a much richer phenomenology [29–36]. Ultracold atoms with SO coupling cannot only shed light on the outstanding problems of condensed matter physics, but also yield completely new phenomena without the analogue elsewhere in physics [37–40].

In this paper, we review the experiments of SO coupling in ultracold gases in our lab. There are three main results in our experiment. Firstly, we experimentally create the effective vector gauge potential for BEC of $^{87}$Rb in the $F = 2$ hyperfine ground state by using two crossed 1064 nm optical dipole trap lasers as the Raman beams. Since rubidium has 15 nm energy-level spitting in the excited-state fine structure, the moderate strength of the Raman coupling with larger one-photon detuning than the excited-state fine structure still can be achieved. We prepare different dressed states in upper and lower branches using three adiabatically loading paths by ramping the homogeneous bias magnetic field and study the different property of the dressed states. Then we observe experimentally, for the first time, the SO coupling in atomic Fermi gas $^{40}$K and investigate the spin dephasing in spin dynamics and momentum distribution asymmetry of the equilibrium state which are the hallmarks of SO coupling in a Fermi gas. From momentum distribution and momentum-resolved radio-frequency (RF) spectroscopy, we observe the change of fermion population in different helicity branches, which indicates that a Lifshitz transition of the Fermi surface topology change can be found by further cooling the system. Inspired by above experiments, we study the momentum-resolved Raman spectroscopy of an ultracold Fermi gas in non-interacting regime and strong interaction regime near a Feshbach resonance. In near Feshbach resonance, we measure the binding energy of Feshbach molecules from a two-component Fermi gas with the momentum-resolved Raman spectroscopy. Comparing with the RF spectroscopy, the signal of unpaired

(free atoms) and the bound molecules can be directly observed and the binding energy can be simultaneously determined in a single running experiment.

## 2 Generation of SO coupling in BEC $^{87}$Rb

In this section, two important parts about SO coupling BEC are involved.

### 2.1 Experiment setup for SO coupling

In our experiment, the basic cooling experiment setup has been described in our previous works [41–45]. The atomic sample $^{87}$Rb atoms in hyperfine state $|F = 2, m_F = 2\rangle$ are first precooled to 1.5 μK by RF evaporative cooling in a quadrupole-Ioffe configuration (QUIC) trap. Subsequently, the atomic gas is transferred non-adiabatically back to the center of the glass cell over a distance of 12 mm in horizontal direction in favor of the optical access. And then loading atoms into an off-resonance dipole trap with the full powers (900 mW and 1.3 W) at a weak homogeneous bias magnetic field about 1 G, the forced evaporative cooling is performed by lowering the powers in three steps. With the total evaporation time of 1.2 s, the pure BEC with the atomic number of $2 \times 10^5$ is obtained at the powers of 169 mW (beam 1) and 320 mW (beam 2). In order to change the Raman coupling strength, the powers of two dipole trap beams are increased to desired value, the pure BEC is still maintained in the dipole trap.

Now we illustrate two important parts in the experimental setup for SO coupling, as shown in Fig. 1. The first is about the Raman coupling laser beams. We use two crossed 1064 nm laser beams for optical dipole trap and the Raman coupling, which are at 90° along $\hat{y} \pm \hat{x}$ and overlapped at the focus, whose polarization are linear and horizontal in the plane of $x$–$y$. They are extracted from a 15 W laser (MOPA 15 NE, InnoLight Technology, Ltd.) operating at the wavelength of 1064 nm with the narrow linewidth single-frequency, and frequency shifted –100 MHz and –110.4 MHz by single passing through two acousto–optic modulators (AOM) (3110-197, Crystal Technology, Inc.) controlled by two signal generators (N9310A, Agilent) respectively. The frequency difference $\nu_R = h \times 10.4$ MHz of two signal generators are phase-locked by a source locking CW microwave frequency counters (EIP 575B, Phase Matrix Inc.). Thus they are phase-locked and frequency shifted 10.4 MHz relative to each other to avoid any spatial interference between the two beams. The most important is that the shifted frequency provide the RF Raman coupling between two magnetic sublevels and can be precisely controlled at the level of Hz. Then the beams are transported to glass cell by two high power polarization maintaining single-mode fibers in order to increase stability of the beam pointing and obtain better beam-profile quality. Behind the fibers, two beams are focused to a waist size of $1/e^2$ radii of 38 μm and 49 μm by achromatic lens. For enhancing the intensity stability, we used two photodiode detectors after reflect mirrors to get the signal of laser intensity, which is compared with a set voltage value by the regulator. The non-zero error signal is compensated by adjusting the RF power in the AOM in front of the optical fibers.

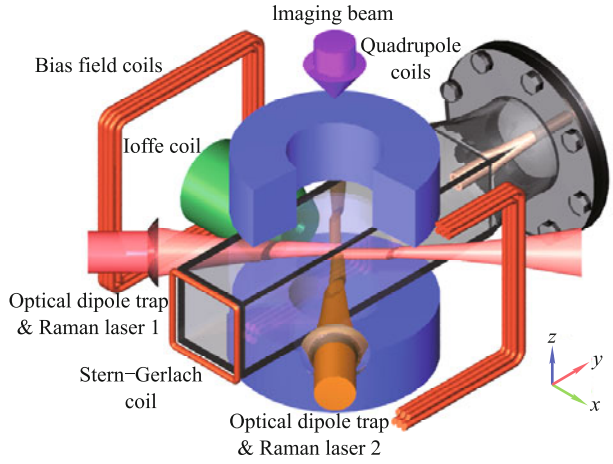


**Fig. 1** Schematic drawing of the experimental setup for SO coupled BEC. Two horizontal crossed beams at 90° are used as the optical dipole trap and the Raman beams.

The other one is about the homogeneous bias magnetic field. It is provided by a pair of Helmholtz coils (the orange coils along $\hat{x}$ in Fig. 1) gives a Zeeman energy split $\omega_Z$ between two magnetic sublevels. A power supply (Delta SM70-45D) operating in remote voltage programming mode is used for coils, whose voltage is set by an analog output of the experiment control system. To control the magnetic field precisely and reduce the magnetic field noise, the current through the coils is controlled by the external regulator relying on a precision current transducer (Danfysik ultastable 867-60I). The output error signal from the regulator actively stabilize the current with the PID (proportional-integral-derivative) controller acting on the MOSFET (metal-oxide-semiconductor field-effect transistor). In order to reduce the current noise and decouple the control circuit from the main current, a conventional battery is used to power the circuit.

### 2.2 Prepare different dressed states

The momentum transfer in the Raman process is $2k_0 =$

$2k_r \sin(\theta/2)$, where $k_r = 2\pi\hbar/\lambda$ is the single-photon recoil momentum, $\lambda$ is the wavelength of the Raman beam, and $\theta$ is the angle between two Raman beams. The recoil energy $E_r = k_0^2/(2m)$. The two photon detuning $\delta \equiv \nu_R - \omega_Z$. The Raman process is described by single particle Hamiltonian [21]

$$H = \begin{pmatrix} \frac{1}{2m}(\boldsymbol{p} - k_0\widehat{e}_x)^2 - \delta/2 & \Omega/2 \\ \Omega/2 & \frac{1}{2m}(\boldsymbol{p} + k_0\widehat{e}_x)^2 + \delta/2 \end{pmatrix}$$
$$= \frac{1}{2m}(\boldsymbol{p}^2 + k_0^2)\check{1} + \frac{\Omega}{2}\sigma_x - (\frac{k_0 p_x}{m} + \frac{\delta}{2})\sigma_z \quad (1)$$

Here, $p_x$ denotes the quasi-momentum of atoms, which relates to the real momentum $k_x$ as $k_x = p_x \mp k_0$ with $\mp$ for spin-up and down, respectively, and $\Omega$ is the strength of the Raman coupling. The "effective Zeeman field" is expressed as $h_p = (\Omega/2, 0, -(k_0 p_x/m + \delta/2))$ at each quasi-momentum, and $\sigma_{x,z}$ is Pauli matrices. This Hamiltonian can be interpreted as an equal weight combination of Rashba-type and Dresselhaus-type SO coupling. $H$ may be diagonalized to get two energy eigenvalues $E_\pm(p_x) = \{(p_x^2 + k_0^2)/2m \pm \sqrt{[4p_x k_0/(2m) - \delta]^2 + \Omega^2}/2\}$, which give the effective dispersion relations of the dressed states. The two dressed eigenstates are expressed by

$$|\uparrow', p_x\rangle = c_1|\uparrow, k_x = p_x + k_0\rangle + c_2|\downarrow, k_x = p_x - k_0\rangle$$
$$|\downarrow', p_x\rangle = c_3|\uparrow, k_x = p_x + k_0\rangle + c_4|\downarrow, k_x = p_x - k_0\rangle \quad (2)$$

Here, $c_1 = 1/\sqrt{a^2+1}$, $c_2 = a/\sqrt{a^2+1}$, and $a = -\{4p_x k_0/(2m) - \delta - \sqrt{[4p_x k_0/(2m) - \delta]^2 + \Omega^2}\}/\Omega$. $c_3 = 1/\sqrt{b^2+1}$, $c_4 = b/\sqrt{b^2+1}$, and $b = -\{4p_x k_R/(2m) - \delta + \sqrt{[4p_x k_0/(2m) - \delta]^2 + \Omega^2}\}/\Omega$. $|\uparrow', p_x\rangle$ is the high-energy dressed state for $E_+(p_x)$ and $|\downarrow', p_x\rangle$ is the low-energy dressed state for $E_-(p_x)$. Since the high and low energies $E_\pm$ of the dressed states depend on the experimental parameters $\Omega$ and $\delta$, the positions of energy minima ($p_{\min}$) are thus experimentally tunable. For $\Omega < 4E_r$ and small $\delta$, the lowest energy $E_-(p_x)$ consists of double wells in quasi-momentum space. As $\Omega > 4E_r$, the double wells merge into a single well.

First we measure the resonant Raman Rabi frequency $\Omega$ by observing population oscillations as a function of Raman pulse time. In experiment, third dipole trap beam (beam 3) with frequency shifted –103 MHz counter-propagating with the Raman beam 2 is used in the measurement process. The BEC in $|\uparrow\rangle = |F = 2, m_F = 2\rangle$ state is transformed adiabatically from initial dipole trap to a new crossed dipole trap composed of Raman beam 1 and dipole trap beam 3 by increasing the power of the dipole trap beam 3 and decreasing the intensity of the Raman beam 2 to zero simultaneously. Then the homogeneous bias magnetic field is ramped to the value with $\delta = -4E_r$, so the atoms are resonant for two dressed states $|\uparrow', -k_0\rangle \rightarrow |\downarrow', -k_0\rangle$ (the energy gap $E_+(p_x = -k_0) - E_-(p_x = -k_0) = \Omega$). By varying Raman pulse length of Raman beam 2 and fitting the population oscillations to the expected behavior, we obtain oscillation period of 420 μs corresponds to the resonant Raman Rabi frequency $\Omega = 2.35E_r$.

Here, when the atoms are Raman resonant (at 10.4 MHz with $\delta = 0$) between $|\uparrow\rangle = |F = 2, m_F = 2\rangle$ and $|\downarrow\rangle = |2, 1\rangle$, the detuning between $|\downarrow\rangle$ and $|F = 2, m_F = 0\rangle$ is about $-30E_r$, so we can neglect the effect of $|F = 2, m_F = 0\rangle$ and regard the system as the two-level model. We adiabatically load the BEC initially in $|\uparrow\rangle$ into the Raman-dressed states of the low $E_-$ or high energy $E_+$ by ramping the homogeneous bias magnetic field with the different paths [22]. At last, the Raman dressed states may be characterized by the time-of-flight (TOF). When the Raman beams and the homogeneous bias magnetic field are turned off abruptly, the atoms are projected onto its individual spin and momentum components. The atoms then expand in a magnetic field gradient for 28 ms during TOF along $\hat{y}$, and the two spin states are separated spatially due to the Stern–Gerlach effect. Imaging the atoms after a 30 ms TOF gives the momentum and spin composition of the dressed state. Now we discuss three cases of loading the BEC into the Raman-dressed states by ramping the homogeneous bias magnetic field with three different paths.

*Case 1*: We prepare the BEC initially in $|\uparrow, 0\rangle$ locating in the low energy branch $E_-$ with the far positive detuning $\delta \gg E_r$ by setting the homogeneous bias magnetic field at the value of $B \ll B_0$, as shown in Fig. 2(a) and (b). Here, $B_0$ corresponds to the $\delta = 0$. Then we ramp the homogeneous bias magnetic field slowly in a time 150 ms to the value with $\delta = 2E_r$ and hold on in a variable time $t_h$. Since $\Omega < 4E_r$ in the experiment, the low energy $E_-(p)$ presents the double wells in quasi-momentum space. When $\delta = 2E_r$, the double wells become asymmetry and the low-energy well locates at $p_{\min} = -0.925k_R$. Thus the atoms are loaded to low-energy dressed state adiabatically and locate low-energy well of the double wells at $p_{\min} = -0.925k_R$. Figure 2(e) shows spin-resolved TOF images of adiabatically loaded the dressed state with the different holding times. These images demonstrate that the atoms are loaded to low-energy dressed state adiabatically at the low-energy well of the double wells, which are very stable with the long-life time.

*Case 2*: The initial condition is same as the case 1. The difference is that the homogeneous bias magnetic field is ramped to the value with $\delta = -E_r$ ($B > B_0$) as

shown in Figs. 2(a) and (c). The low-energy well of the asymmetry double wells is changed into $p_{\min} = 0.889k_0$. The atoms still are loaded to low-energy dressed state adiabatically, however locate at high-energy well (no $p_{\min}$) of the double wells as shown Fig. 2(c). The dressed atoms locating at high-energy well of the double wells are unstable and will transit to the low-energy well. Images in Fig. 2(f) show this transition process. After holding time of 20 ms, the dressed atoms populate the low-energy well of the double wells.

*Case 3*: We prepare the BEC initially in $|\uparrow, 0\rangle$ locating in the high energy branch $E_+$ with the far negative detuning $\hbar\delta \ll -E_r$ by setting the homogeneous bias magnetic field at the value of $B > B_0$, as shown in Figs. 2(a) and (d). The homogeneous bias magnetic field is decreased to the value with $\delta = -7E_r$ and the atoms are loaded to high-energy dressed state adiabatically. The high energy branch $E_+(p)$ consists of single well in quasi-momentum space, thus the dressed atoms locate at $p_{\min} = -0.84k_R$. The dressed atoms in high quasibands are energetically allowed, however, collisional decay will be present near Raman resonance except the lowest-energy dressed state [46]. The decay for variable hold times ranging from 1 ms to 19 ms is observed as shown in Fig. 4(c). The dressed atoms in higher branch decay into the low-energy band accompanying the heating, which is a completely different process compared with that of case 2. In Ref. [47], Zhang and coworkers carried out a thorough and quantitative study of the decay behavior of excited dressed states with SO coupling and find two SO-coupling-induced decay mechanisms, one arises from single-atom motion in inhomogeneous trap potential and the other from two-body interatomic collisions. The stability analysis showed how to control the stability of excited dressed state with SO coupling.

## 3 Realization of SO coupled Fermi gas $^{40}$K

While SO coupled bosonic gases were generated experimentally with much excitement, Fermi gases hold even more promise. Due to the Pauli exclusion principle, fermions occupy a large number of momentum states, and are therefore sensitive to global (topological) features of the band structure. Conversely, BEC typically occurs in one or two single-particle states. SO coupled fermionic gases would thus provide ways to explore a much richer phenomenology. One can envision that this technique may be combined with Feshbach resonances which control the interatomic interactions and optical lattices or disorder potential which mimic the phenomenon in real materials, enabling the production of exotic states found in condensed-matter systems such as topological insulators. Even more importantly, many schemes were proposed to realize novel states of matter in these SO coupling Fermi gases [48–52], e.g., fractional topological insulators, Majorana fermions, and topological edge spins, which are anticipated by many

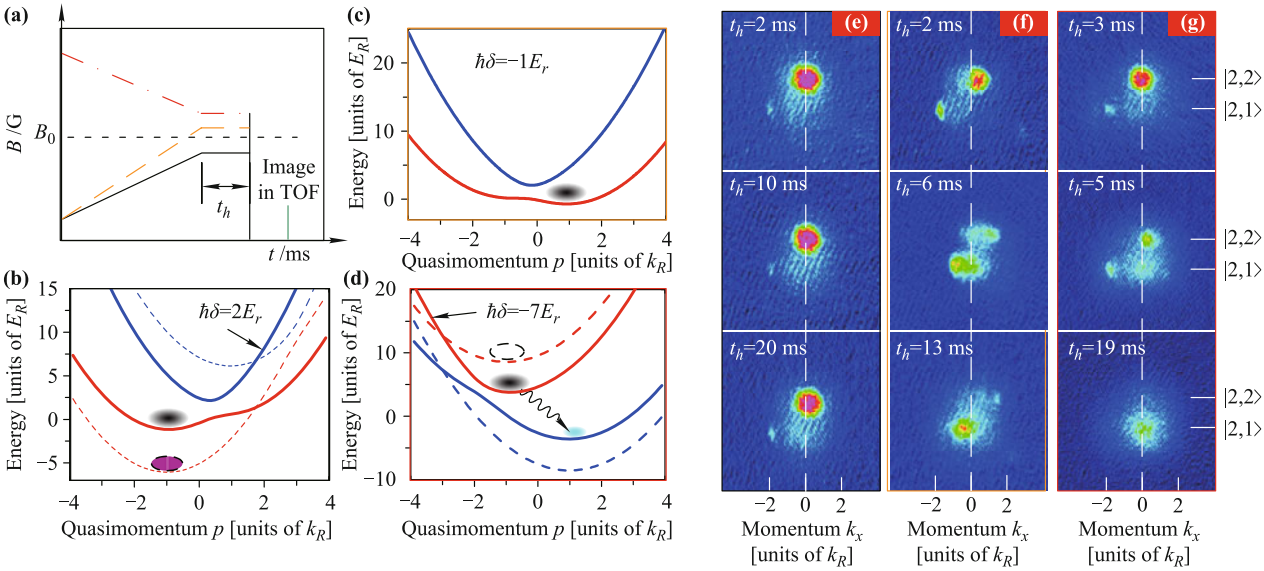


**Fig. 2** Experimental sequence, energy-quasimomentum dispersion and TOF images for loading BEC into different Raman-dressed states. **(a)** The time sequence of the homogeneous bias magnetic field for loading the atoms into lower Raman-dressed state with detuning $\hbar\delta = 2E_r$ (*black solid line*) and $\hbar\delta = -1E_r$ (*orange dashed line*), and high-energy Raman-dressed state with detuning $\hbar\delta = -7E_r$ (*red dot dashed line*). The horizontal dashed line indicates $B_0$, which corresponds to $\delta = 0$. **(b, c, d)** Energy-quasimomentum dispersion for different final dressed state with the detuning $2E_r$, $-1E_r$, and $-7E_r$ respectively. **(e, f, g)** The corresponding TOF images (1.17 mm by 1.17 mm) of the Raman-dressed state with detuning $2E_r$, $-1E_r$, and $-7E_r$ after variable hold times $t_h$. The two spin and momentum components are spatially separated along $\hat{y}$.

theoretical studies but are hard to create and analyze experimentally in condensed matter physics.

### 3.1 Experiment setup

The experimental procedure starts with a degenerate Fermi gas of about $N \simeq 2 \times 10^6$ $^{40}$K atoms in the $|9/2, 9/2\rangle$ internal state, which has been evaporatively cooled with bosonic $^{87}$Rb atoms in the $|F = 2, m_F = 2\rangle$ state inside a crossed optical trap as shown in Fig. 3(a). The optical dipole trap is composed of two horizontal crossed beams of 1064 nm along the $\hat{x} \pm \hat{y}$ direction overlapped at the focus, which is identical to the above case of Bose gas. The temperature of the Fermi gas is about 0.3 $T_F$ ($T_F$ is the Fermi temperature) when the trap frequency reaches $2\pi \times (116, 116, 164)$ Hz along the $(\hat{x}, \hat{y}, \hat{z})$ direction. A pair of Helmholtz coils provides a homogeneous bias magnetic field along $\hat{y}$ (quantization axis).

In the $^{40}$K system, two spin states are chosen as two magnetic sublevels $|\uparrow\rangle = |F = 9/2, m_F = 9/2\rangle$ and $|\downarrow\rangle = |F = 9/2, m_F = 7/2\rangle$. They are coupled by a pair of Raman beams derived from a Ti:Sapphire laser with the wavelength 773 nm, the frequency difference $\nu_R$, and the coupling strength $\Omega$. Two Raman lasers counterpropagate ($k_0 = k_r$) along the $\hat{x}$ axis and are linearly polarized along the $\hat{y}$ and $\hat{z}$ directions, respectively, corresponding to $\pi$ and $\sigma$ polarization relative to quantization axis $\hat{y}$, as shown in Fig. 3(a). Other magnetic Zeeman sublevels can be neglected because the the detuning is 1 order of magnitude larger than the Fermi energy. Finally, before TOF measurement, the Raman beams, optical dipole trap and the homogeneous bias magnetic field are turned off abruptly at the same time, and a magnetic field gradient along $\hat{y}$ direction provided by Ioffe coil is turned on. Two spin states are separated along $\hat{y}$ direction, and imaging of atoms along $\hat{z}$ direction after 12 ms expansion gives the momentum distribution for each spin component.

We first study the Rabi oscillation between the two spin states induced by the Raman coupling. All atoms are initially prepared in the $|\uparrow\rangle$ state. The homogeneous bias magnetic field is ramped to a certain value and $\delta = -4E_r$ where the $k = 0$ component of state $|\uparrow\rangle$ is at resonance with the $k = 2k_r\hat{e}_x$ state of the $|\downarrow\rangle$ component. Then we apply a Raman pulse to shine the atomic gas and measure the spin population for different duration time of the Raman pulse. As we know, a similar experiment in the boson system yields an undamped and completely periodic oscillation, which can be well described by a sinusoidal function with frequency $\Omega$. This is because, for bosons, a macroscopic number of atoms occupy the resonant $k = 0$ mode, and therefore there is a single

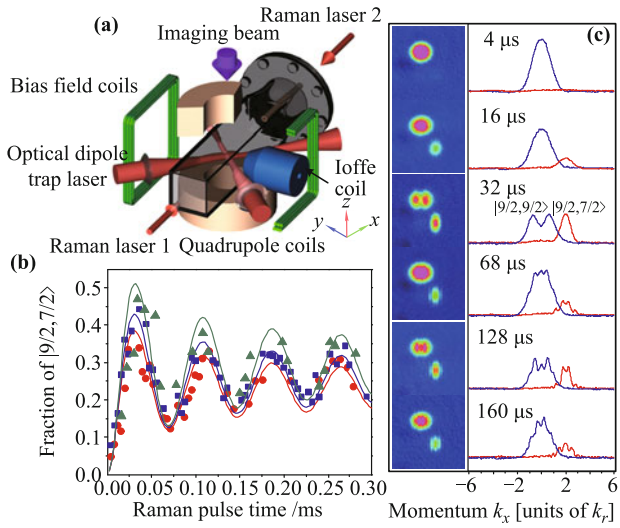


**Fig. 3** Experimental setup and Raman-induced quantum spin dynamics. **(a)** Schematic of the experimental setup, a pair of Raman beams are counterpropagating along $\hat{x}$. **(b)** The population in $|9/2, 7/2\rangle$ as a function of duration time of the Raman pulse. $k_F = 1.9k_r$ and $T/T_F = 0.3$ for red circles, $k_F = 1.35k_r$ and $T/T_F = 0.35$ for blue squares, and $k_F = 1.1k_r$ and $T/T_F = 0.29$ for green triangles. The solid lines are theory curves with $\Omega = 1.52(5)E_r$. **(c)** With the different duration times at $k_F = 1.35k_r$ and $T/T_F = 0.35$, we show TOF image (left) and integrated time-of-flight image (integrated along $\hat{y}$) for $|\uparrow\rangle$ (*blue*) and $|\downarrow\rangle$ (*red*).

Rabi frequency determined by the Raman coupling only, while, for fermions, atoms occupy different momentum states. Precisely due to the effect of SO coupling, the coupling between the two spin states and the resulting energy splitting are momentum dependent, and atoms in different momentum states oscillate with different frequencies.

To determine the value of $\Omega$ from the measurements, we fix Raman coupling and vary atomic density by changing the total number of fermions or the trapping frequency, and we obtain several different oscillation curves, as shown in Fig. 3(b). Then we fit them to the theory with a single fitting parameter $\Omega$. Theoretically, for a noninteracting system, the population of the $|\downarrow\rangle$ component is given by

$$n_\downarrow(k + 2k_r\hat{e}_x, r, t) = n_\uparrow(k, r, 0)\frac{\sin^2\sqrt{(k_x k_r/m)^2 + \Omega^2/4}t}{1 + \left(\frac{2k_x k_r}{\Omega m}\right)^2} \quad (3)$$

where $t$ is the duration time of the Raman pulse, $n_\uparrow(k, r, 0)$ is the equilibrium distribution of the initial state in the local density approximation. The theoretical expectation of the total population in the $|\downarrow\rangle$ component is given by $\boldsymbol{N}_\downarrow = \int \mathrm{d}^3\boldsymbol{k}\mathrm{d}^3\boldsymbol{r}n_\downarrow(k, r, t)$, from the experimental data [shown in Fig. 3(c)] and theory, we determine $\Omega = 1.52(5)E_r$. Our current experiment is

performed in the weakly interacting regime with s-wave scattering length of $a_s = 169a_0$, we have verified that the interaction effect is negligible.

### 3.2 Momentum distribution and Lifshitz transition

With SO coupling, the single particle spectra are dramatically changed from two parabolic dispersions in the case of non interacting two component Fermi gas into two helicity branches. Here, two different branches are eigenstates of "helicity" $\hat{s}$, and the helicity operator describes whether spin $\sigma_p$ is parallel or antiparallel to the "effective Zeeman field" $h_p = (-\Omega, 0, k_r p_x/m + \delta)$ at each momentum. $\hat{s} = \sigma_p \cdot h_p/|\sigma_p \cdot h_p| = 1$ for the upper branch, and $-1$ for the lower branch.

We firstly focus on the case with $\delta = 0$ and study the momentum distribution in the equilibrium state with different fermion density, as shown in Fig. 4. Since SO coupling breaks spatial reflectional symmetry ($x \to -x$ and $k_x \to -k_x$), the momentum distribution for each spin component will be asymmetric. On the other hand, when $\delta = 0$ the different spin component still satisfies $n_\uparrow(k) = n_\downarrow(-k)$, but for the same spin component $n_\uparrow(k) = n_\uparrow(-k)$. The property can be clearly seen in the spin-resolved TOF images [shown in Figs. 4(a) and (b)] and integrated distributions [shown in Figs. 4(d) and (e)]. While the asymmetry becomes less significant when the fermion density becomes higher, as shown in Figs. 4(c) and (f), because the strength of SO coupling is relatively weaker compared to the Fermi energy.

We also study the topology of the Fermi surface, which exhibits two transitions as the atom density varies. At sufficiently low density, it contains two disjointed Fermi surfaces with $s = -1$, and they gradually merge into a single Fermi surface as the density increases to $n_{c1}$. Finally, a new small Fermi surface appears at the center of the large Fermi surface when density further increases and fermions begin to occupy the $s = 1$ helicity branch at $n_{c2}$, as shown in Fig. 5(c). Across the phase boundaries, the system experiences Lifshitz transitions as the density increases, which is a unique property in a Fermi gas due to the Pauli principle.

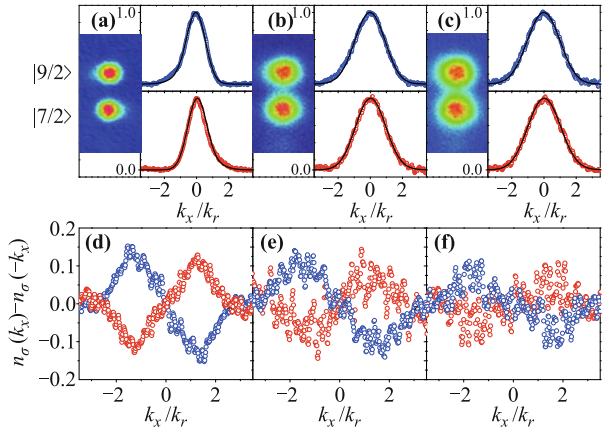


**Fig. 4** Momentum distribution asymmetry as a hallmark of SO coupling: **(a)–(c)** time-of-flight measurement of momentum distribution for both $|\uparrow\rangle$ (*blue*) and $|\downarrow\rangle$ (*red*). Solid lines are theory curves. (a) $k_F = 0.9k_r$ and $T/T_F = 0.8$; (b) $k_F = 1.6k_r$ and $T/T_F = 0.63$; (c) $k_F = 1.8k_r$ and $T/T_F = 0.67$. **(d)–(f)** Plot of integrated momentum distribution $n_\sigma(\boldsymbol{k}) - n_\sigma(-\boldsymbol{k})$ for the case of (a)–(c).

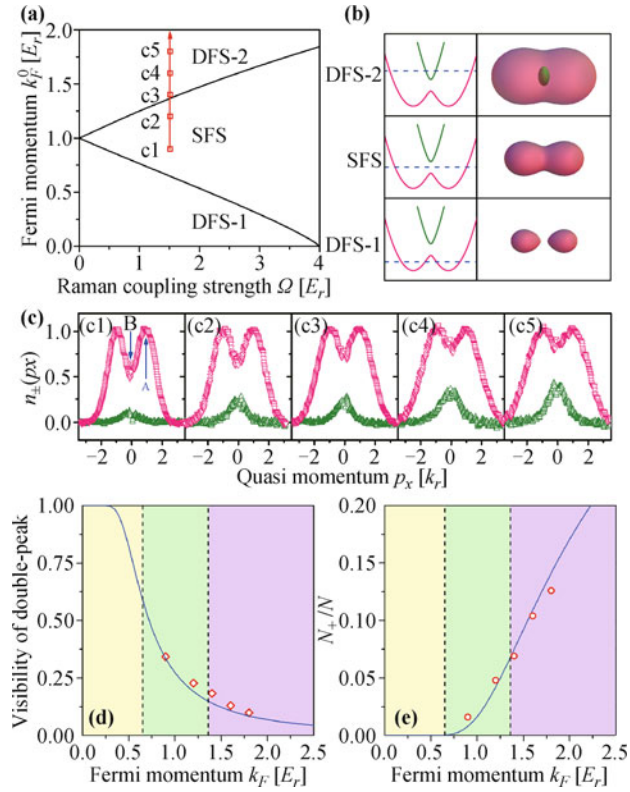


**Fig. 5** Topological change of the Fermi surface and Lifshitz transition. **(a)** Theoretical phase diagram at $\boldsymbol{T} = 0$. "SFS" means single Fermi surface, "DFS" means double Fermi surface. **(b)** Illustration of different topologies of Fermi surfaces. The single particle energy dispersion is drawn for small $\Omega$. The dashed blue line is the chemical potential. **(c)** Quasimomentum distribution in the helicity bases. Red and green points are distributions for the $s = 1$ and $s = -1$ helicity branches, respectively. (c1) $k_F = 0.9k_r$ and $T/T_F = 0.8$; (c2) $k_F = 1.2k_r$ and $T/T_F = 0.69$; (c3) $k_F = 1.4k_r$ and $T/T_F = 0.61$; (c4) $k_F = 1.6k_r$ and $T/T_F = 0.63$; (c5) $k_F = 1.8k_r$ and $T/T_F = 0.57$. **(d)** Visibility $v = (n_A - n_B)/(n_A + n_B)$ decreases as $k_F/k_r$ increases. **(e)** Atom number population in $s = 1$ helicity branch $N_+/N$ increases as $k_F/k_r$ increases. In both (d) and (e), the blue solid line is a theoretical curve with $T/T_F = 0.65$, and the background color indicates three different phases in the phase diagram.

The quasimomentum distribution in the helicity bases can be obtained from a transformation of momentum distribution in spin bases as follows:

$$n_+(\boldsymbol{p}) = \frac{u_{\boldsymbol{p}}^2 n_\uparrow(\boldsymbol{p} - \hbar k_r \hat{\boldsymbol{e}}_x) - v_{\boldsymbol{p}}^2 n_\downarrow(\boldsymbol{p} + \hbar k_r \hat{\boldsymbol{e}}_x)}{u_{\boldsymbol{p}}^2 - v_{\boldsymbol{p}}^2}$$

$$n_-(\boldsymbol{p}) = \frac{v_{\boldsymbol{p}}^2 n_\uparrow(\boldsymbol{p} - \hbar k_r \hat{\boldsymbol{e}}_x) - u_{\boldsymbol{p}}^2 n_\downarrow(\boldsymbol{p} + \hbar k_r \hat{\boldsymbol{e}}_x)}{v_{\boldsymbol{p}}^2 - u_{\boldsymbol{p}}^2} \quad (4)$$

Here, the coefficients $u_{\boldsymbol{p}}^2 = 1 - v_{\boldsymbol{p}}^2 = \frac{1}{2}\left[1 - \frac{p_x v_r - \delta/2}{\sqrt{(p_x v_r - \delta/2)^2 + \Omega^2/4}}\right]$ are only functions of $p_x$ with $v_r = k_r/m$. We plot the quasimomentum distribution in the helicity bases for different atom densities displayed in Fig. 5(c1–c5). At the lowest density, the $s = 1$ helicity branch is nearly unoccupied, which is consistent with the Fermi surface being below the $s = 1$ helicity branch. The quasimomentum distribution of the $s = -1$ helicity branch exhibits clearly a double-peak structure, which reveals that the system is close to the boundary of having two disjointed Fermi surfaces at the $s = -1$ helicity branch. As the density increases, the double-peak feature gradually disappears, indicating that the Fermi surface of $s = -1$ helicity branch finally becomes a single elongated one. In Fig. 5(d), we show that our data decrease as the density increases and agree very well with a theoretical curve for visibility with fixed temperature $T/T_F = 0.65$, the visibility is defined as $\nu = (n_{-1} - n_1)/(n_{-1} - n_1)$, where $n_{\pm 1}$ is the atomic density of the $s = \pm 1$ helicity. Moreover, across the phase boundary between the single Fermi surface and double Fermi surface, one expects a significant increase of population on the $s = 1$ helicity branch. In Fig. 5(e), the fraction of the $s = 1$ helicity branch is plotted as a function of Fermi wave-vector $k_F$. Its rapid growth near the critical point provide a strong evidence that a new Fermi surface emerges, and the curve shows quite good agreement with the theoretical prediction at finite temperature. Because the temperature is so high that the transition is washed out, for both $\nu$ and $N_+/N$ we observe only a smooth decreasing or growth across the regime where it is supposed to have a sharp transition; however, the agreement with theory suggests that with better cooling a sharper transition should be observable. A more accurate experimental determination of Lifshitz transition point requires further cooling of the system.

### 3.3 Momentum-resolved RF spectroscopy for SO coupling

The effect of SO coupling is further studied with momentum-resolved RF spectroscopy. The method is the same as first developed in Ref. [56]. Recently, spin injection spectroscopy has also been applied to study SO coupled Fermi gas by the Massachusetts Institute of Technology group [28]. They focused on lithium-6, which has an unfavorable ratio of excited fine structure splitting. In fact, prior to this study the common wisdom was that inelastic light scattering would make such a study impractical. With an ingenious approach to circumvent this problem, they worked with four atomic states, and used radio waves to drive transitions from two "reservoir" states into two SO coupled states and controlled the heating by keeping the population of the SO coupled states low. By monitoring the transition rate as a function of the RF, they were able to map out the dispersion of the SO coupled states. They also created a SO coupled lattice and probed its spinful band structure, which features additional spin gaps and a fully gapped spectrum.

In our case, a Gaussian shape pulse of the RF pulse is applied for 200 μs to transfer atoms from one of SO coupled states $|\downarrow\rangle = |F = 9/2, m_F = 7/2\rangle$ to a normal state $|F = 9/2, m_F = 5/2\rangle$, as shown in Fig. 6(a), and then the spin population at the final state is measured with TOF. The initial state dispersion can be mapped out by

$$\varepsilon(k) = \hbar\nu_{\mathrm{RF}} - E_Z + \varepsilon_F(k) \quad (5)$$

where $\varepsilon_F(k)$ is the dispersion for the final state $|9/2, 5/2\rangle$ and $E_Z$ is the Zeeman energy difference between the $|9/2, 7/2\rangle$ and $|9/2, 5/2\rangle$ states. In Fig. 6(b), we plot an example of the final state population as a function of momentum $p_x$ and the frequency of applied RF field, from which one can clearly see the back-bending feature and the gap opening at the Dirac point. Both are clear evidence of SO coupling. In Figs. 6(c), (d), and (e), we show three measurements corresponding to (c1), (c3), and (c5) in Fig. 5. For (c), clearly only the $s = -1$ branch is populated. For (d), the population is slightly above the $s = -1$ helicity branch. And for (e), there is already significant population at the $s = 1$ helicity branch. In Fig. 5(c5), one can also identify the chiral nature of two helicity branches. For the $s = -1$ branch, most left-moving states are dominated by the $|\downarrow\rangle = |F = 9/2, m_F = 7/2\rangle$ state, while for the $s = 1$ branch, right-moving states are mostly dominated by $|\downarrow\rangle$ states.

We also study the momentum-resolved RF spectroscopy for the case with Raman detuning $-1E_r$. In Fig. 6(f), the dispersion and spin texture of the two branches are obtained from the measured data with detuning $\delta = -1E_r$. There are double wells with different minimum energy, and we can find that the spin down fermions can mainly occupy in the right well with positive quasimomentum. And there is also some Fermions already populating at the $s = 1$ helicity branch.

## 4 Momentum-resolved Raman spectroscopy for Fermi gas

Inspired by the above experiment, we study the

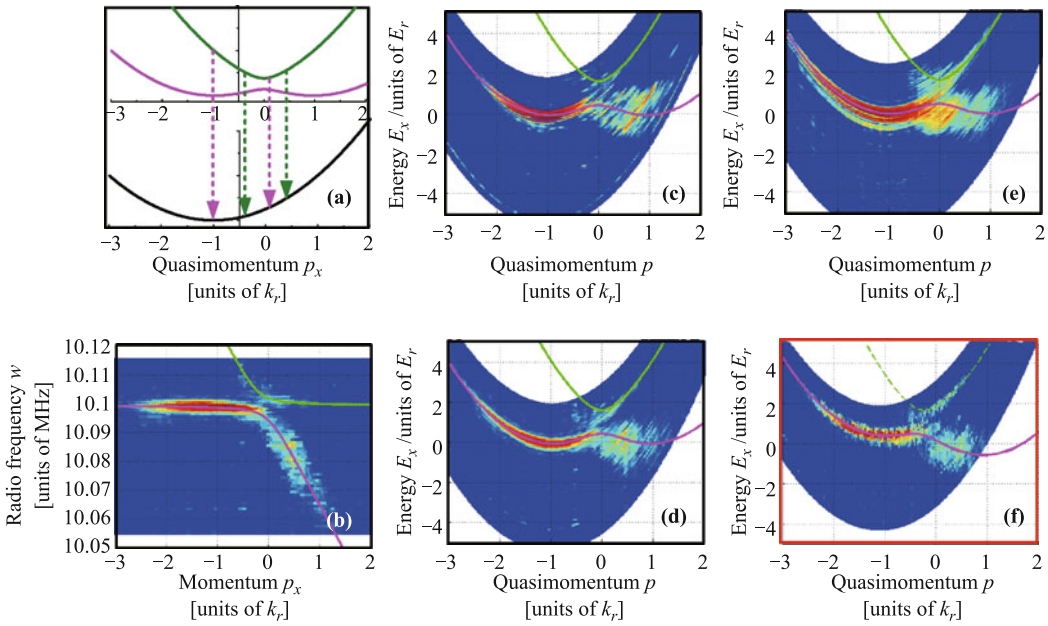


**Fig. 6** Momentum-resolved RF spectroscopy of SO coupling Fermi gases. **(a)** Schematic of momentum-resolved RF spectroscopy of SO coupled Fermi gases. Green and pink solid lines are two helicity branches in which the eigenstates are all superpositions of $|F = 9/2, m_F = 9/2\rangle$ and $|9/2, 7/2\rangle$. Thus both can undergo RF transition from $|9/2, 7/2\rangle$ to $|9/2, 5/2\rangle$, as indicated by dashed lines. **(b)** Intensity map of the atoms in the $|9/2, 5/2\rangle$ state as a function of the $(v_{\rm RF}, k_x)$ plane. **(c, d, e)** Single particle dispersion corresponding to atomic population of (c1), (c3), and (c5) in Fig. 5. **(f)** the momentum-resolved RF spectroscopy for the case with detuning $-1E_r$.

momentum-resolved Raman spectroscopy of an ultracold Fermi gas in non-interacting regime and strongly interaction near Feshbach resonance [53, 54]. As we know, many tools have been proposed and used to study strongly interacting ultracold atomic gases such as the spatial noise correlations [57, 58], RF spectroscopy [55, 56, 59–63], momentum-resolved stimulated Raman technique [64, 65] and Bragg spectroscopy [66, 67].

Raman spectroscopy is an important tool similar to RF spectroscopy. RF spectroscopy can be regarded as a special case of Raman spectroscopy with a vanishing transferred momentum. In the stimulated Raman process, atoms are transferred into a different internal state by absorbing a photon from a laser beam and immediately reemitting it into another laser beam with different frequency and wave vector. The several significant advantages compared to the RF spectroscopy are described [65], e.g., spatial selectivity to eliminate inhomogeneous broadening due to the trap potential, tunability of the transferred momentum from below to well above the Fermi momentum, and weaker sensitivity to final-state interactions. An interesting advantage shown in Ref. [54], bound molecules can be directly observed and the binding energy can be simultaneously determined in a single running experiment using momentum-resolved Raman spectroscopy.

To obtain the Raman spectroscopy, two $\lambda = 773$ nm laser beams counterpropagating along the $\hat{x}$ axis are linearly polarized along $\hat{y}$ and $\hat{z}$, corresponding to $\pi$ and $\sigma$ relative to quantization axis $\hat{y}$, as shown in Fig. 7(a). Both beams are extracted from a Ti:sapphire laser operating at 773 nm and focused onto the ultracold atomic sample with $1/e^2$ radii of 200 μm, which is larger than the atomic cloud size. Two Raman beams are frequency-shifted by single-pass through two AOM driven by two signal generators respectively. The frequency difference is adjusted by changing the frequency of the signal generator. We apply a Raman laser pulse with intensity $I = 50$ mW for each laser beam, duration time of 35 μs, which is much smaller than the optical trap period. After the Raman pulse, we then immediately turn off the optical trap and the homogeneous magnetic field, let the atoms ballistically expand in 12 ms and take the TOF absorption image on a CCD (charge-coupled device). In order to measure the fraction of atoms in different Zeeman states, a gradient magnetic field along $\hat{y}$ direction is applied with 10 ms during the TOF. The atoms in two spin states are separated spatially due to the Stern–Gerlach effect.

Considering the energy and momentum conservation in the Raman process, we therefore obtain that

$$\hbar\Delta\omega = E_Z + \epsilon_{\uparrow}^{\rm Initial}(\boldsymbol{k}) - \epsilon_{\downarrow}^{\rm Final}(\boldsymbol{k} + 2\boldsymbol{k}_0) \qquad (6)$$

where $\epsilon_{\uparrow}^{\rm Initial}(\boldsymbol{k})$ and $\epsilon_{\downarrow}^{\rm Final}(\boldsymbol{k} + 2\boldsymbol{k}_0)$ are energy–momentum dispersion of the spin up and down states respectively. From this, we can determine the energy-momentum dispersion of the initial state if the

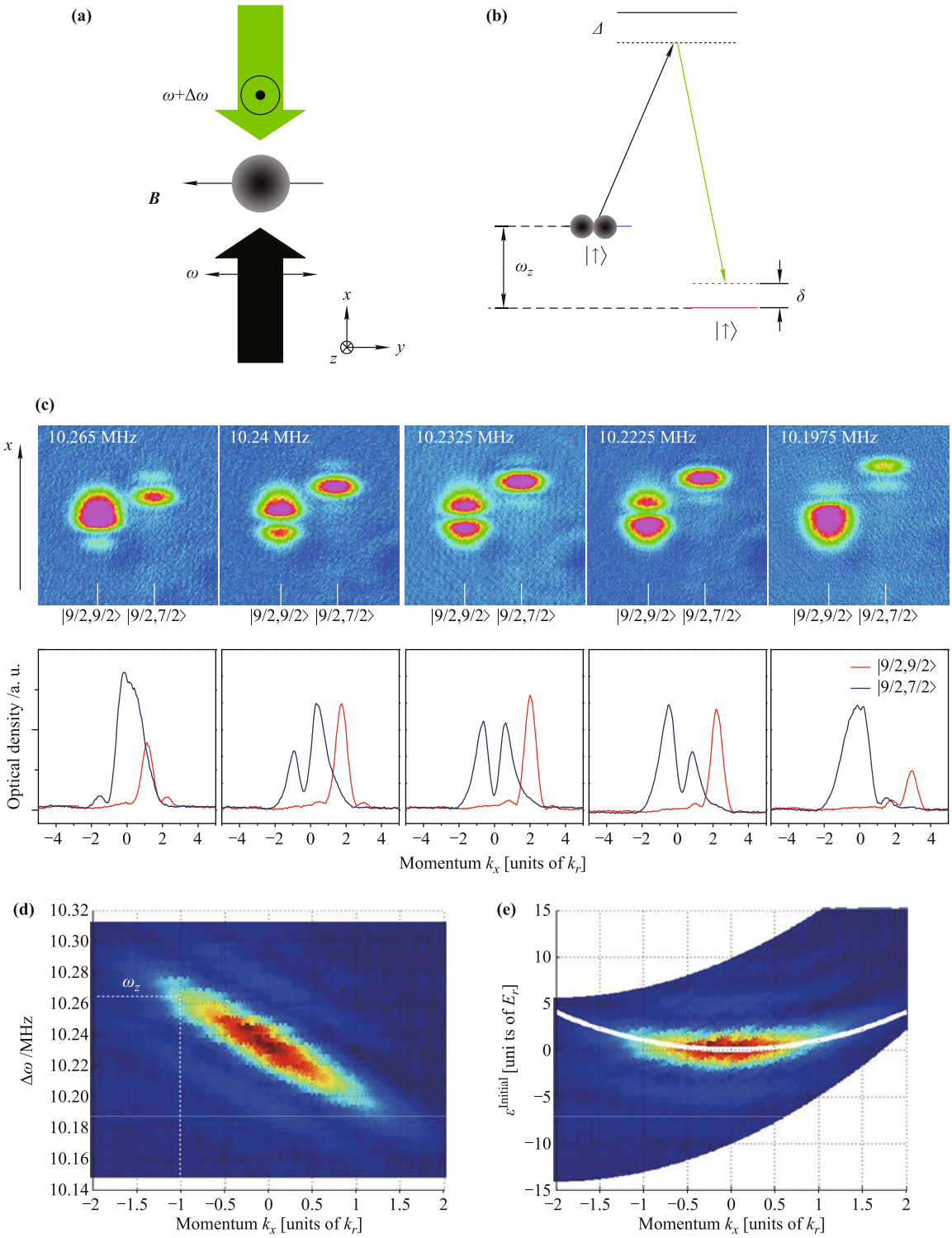


**Fig. 7** Experiment of Raman spectroscopy in non interacting case. **(a)** Schematic of the Raman spectroscopy. The two Raman beams counterpropagate along $\pm\hat{x}$ with frequency $\omega$ and $(\omega + \Delta\omega)$, linearly polarized along $\hat{y}$ and $\hat{z}$, correspond to $\pi$ and $\sigma$ relative to the quantization axis $-\hat{y}$. **(b)** The Raman transition with a Zeeman shift $\omega_Z$ and a detuning $\delta$ from the Raman resonance. **(c)** The absorption images of two Zeeman states after 12 ms TOF for different Raman frequency detuning. **(d)** Plot is intensity map of the atoms in the $|\downarrow\rangle$ state in the $(\Delta\omega, k_x)$ plane. **(e)** The translated intensity shows the atom number as a function of the single particle energy (normalized to $E_r$) and momentum $k_x$ (normalized to $k_r$). The white line is the expected quadratic dispersion curve.

energy–momentum dispersion of the final state is known (for example, $\epsilon_{\downarrow}^{\mathrm{Final}}(\boldsymbol{k}) = \boldsymbol{k}^2/(2m)$ for the finial state with the non-interaction)

$$\epsilon_{\uparrow}^{\mathrm{Initial}}(\boldsymbol{k}) = \hbar\Delta\omega - E_Z + \epsilon_{\downarrow}^{\mathrm{Final}}(\boldsymbol{k} + 2\boldsymbol{k}_0) \tag{7}$$

In case of the non-interaction fermion gas, the energy-momentum dispersions of the initial and final states present the quadratic function with $\epsilon_{\uparrow} = \epsilon_{\downarrow} = \boldsymbol{k}^2/(2m)$. Thus, Eq. (6) becomes

$$\hbar\Delta\omega = E_Z - \frac{4\boldsymbol{k}_0^2}{2m} - \frac{2\boldsymbol{k}_0 \cdot \boldsymbol{k}}{m} \tag{8}$$

Since the parameters $E_Z$ and $\boldsymbol{k}_0$ are fixed in experiment, it is linear relationship between the frequency difference of two Raman beams and the atomic momentum.

For the non-interacting case, all $^{40}$K atoms are initially prepared in the $|F = 9/2, m_F = 9/2\rangle$ state (spin up state) and the final state $|F = 9/2, m_F = 7/2\rangle$ is empty. The homogeneous bias magnetic field is ramped to a certain value, which give an energy splitting of $\omega_Z/2\pi \simeq 10.265$ MHz between Zeeman states $|9/2, 9/2\rangle$ and $|9/2, 7/2\rangle$. Then we apply a Raman pulse with 35 μs to the system, and measure the spin population for different frequency detuning of the Raman lasers, as shown in Fig. 7(c). As we can see, only atoms in the certain momentum state are transferred from $|F = 9/2, m_F = 9/2\rangle$ to $|F = 9/2, m_F = 7/2\rangle$, which is determined by the frequency difference of the Raman lasers. It presents the inherent momentum-resolved characteristics of Raman spectroscopy. We integrate TOF image along $\hat{y}$ to obtain the momentum distributions in $\hat{x}$ of two spin states respectively, as shown in Fig. 7(c). The appearance of side lobes in the momentum distributions of the spin state $|9/2, 7/2\rangle$ is due to the square envelop of Raman laser intensity. Then all momentum distributions in $\hat{x}$ of the spin state $|9/2, 7/2\rangle$ for different frequency differences of the Raman lasers are grouped into the $(\Delta\omega, k_x)$ plane, as shown in Fig. 7(d). Note that all momentum distributions in $\hat{x}$ are translated with the two-unit momentum $2k_r$ in Fig. 7(d). The distribution of Fig. 7(d) clearly shows the linear relationship between the atomic momentum and the frequency difference of two Raman beams for non-interaction Fermi gas. According to Eq. (6) and the quadratic energy–momentum dispersion of the final state, the energy–momentum dispersion of the initial state $|9/2, 9/2\rangle$ is obtained from the measured spectrum. Fig. 7(e) shows the distribution of the atom number in the initial spin state as a function of the single particle energy and momentum, which is in good agreement with the expected behavior of the quadratic function.

On the BEC side of Feshbach resonance, the unpaired atoms and bound molecules exist simultaneously. For the unpaired atoms, the dispersion shows the same line like above. For the bound molecules, it does not exhibit exactly quadratic dispersion. Eq. (6) becomes

$$\epsilon_{\uparrow}^{\mathrm{Initial}}(\boldsymbol{k}) = (\hbar\Delta\omega - E_b) - E_Z + \epsilon_{\downarrow}^{\mathrm{Final}}(\boldsymbol{k} + 2\boldsymbol{k}_0) \tag{9}$$

where $E_b$ is the molecular binding energy. Under the effect of Raman process, the bound molecules are broken into two free atoms with equal and opposite momentum in the molecule center-of-mass frame. Residual energy transfer the broken atoms from a spin state ($|9/2, -7/2\rangle$) to the third state ($|9/2, -5/2\rangle$), as shown in Fig. 8(a), which is marked by red arrows. One can observe the signal of unpaired atoms marked by red line in the same absorption images. From the images, we can obtain the distance and position of two peaks by fitting the integrated density curves along $\hat{z}$ direction. Then we prepare an atomic sample in single state ($|9/2, -7/2\rangle$) and search an transferred atomic peak in Raman process with same position of above molecular signal, which corresponds to the frequency difference of two Raman beams $(\hbar\Delta\omega - E_b)$.

We measure the binding energy of molecules $E_b(B)$ versus the magnetic field $B$ on the BEC side of Feshbach resonance in a single running experiment. The Feshbach molecules are created in $^{40}$K atomic gas consisting of an equal mixture of atoms in the $|F = 9/2, m_F = -9/2\rangle$ and $|F = 9/2, m_F = -7/2\rangle$ states by ramping the magnetic field across the s-wave Feshbach resonance 202.1 G to a value below the resonance. Then we apply a Gaussian shape pulse of Raman laser to transfer atoms from the state $|9/2, -7/2\rangle$ to the final state $|9/2, -5/2\rangle$ and record the momentum distribution of the atoms in $|9/2, -5/2\rangle$ state by TOF absorption image. By selecting the appropriate frequency difference of the two Raman beams, the two distinctly different momentum distributions of the atoms in $|9/2, 5/2\rangle$ state along $\hat{x}$ appear in a TOF absorption image as shown in Fig. 8(a). The two peaks is induced by the unpaired atoms and bond molecules with the different momentums, which satisfies simultaneously when fixing frequency difference of two Raman beams. In order to recognize the different momentum distributions, we perform the same procedures, and the only difference is to prepare atoms in the single spin state $|9/2, 7/2\rangle$ instead of the equal mixture. The TOF image only shows a single momentum distribution of the atoms in the $|9/2, 5/2\rangle$ state, which corresponds to the free atoms as shown in Fig. 8(a). The peak corresponding to unpaired atoms is narrower and exhibits symmetric shape. The asymmetric peak corresponds to the dissociation of the bound molecules. This result shows that the composition of gas includes the unpaired atoms and bound molecules in the BEC side.

To determine the binding energy of molecules exactly, we first determine the maximum molecule signal and then fit this curve to extract the distance $x$ of two peaks of the atoms in $|9/2, 5/2\rangle$ state from the atom optical density integration along the $\hat{z}$ direction. The relationship between the binding energy of molecules and the distance $x$ of two peaks can be determined by preparing atoms in the single spin state $|9/2, 7/2\rangle$ and performing respectively two measurements under two frequency differences $\Delta\omega_1$ and $\Delta\omega_2$. The distance between the atomic momentum distribution peaks measured at the two cases and corresponds to the energy $\hbar(\Delta\omega_1 - \Delta\omega_2)$. The function of the molecule binding energy versus the magnetic-field intensity is plotted in Fig. 8(c). The binding energy of molecules can be directly measured in a single running experiment if the binding energy of molecules is smaller than about 70 kHz. When the binding energy of molecules is larger than about 70 kHz, we must perform two measurements to determine the positions of molecules and unpair atoms respectively. Now we reconstruct the spectral function of the Fermi gas on the BEC side by the momentum-resolved Raman spectroscopy which simultaneously presents the characteristics of the unpaired atoms and bound molecules, in which the unpaired atoms shown early quadratic dispersion; however, the bound molecules does not exhibit exactly quadratic dispersion. The bound molecules are broken into two free atoms with equal and opposite momentum in the molecule center-of-mass frame by the Raman laser. Thus there is the extended momentum distribution at the lower negative energy below the binding energy. The broader dispersion of the bound molecules is shown in Fig. 8(e). In Ref. [56], an inverse Abel transform is used to reconstruct the three-dimensional momentum distribution when the momentum distribution is isotropic. Then the dispersion spectra along the radial direction of momentum are obtained. Here, we give the dispersion in the $k_x$ direction after integrating one direction of the absorption image. Although the dispersion spectra between our work and Ref. [56] are plotted with different forms, the dispersion spectra of the bound molecules show similar features since they come from the same wave function of bound molecules.

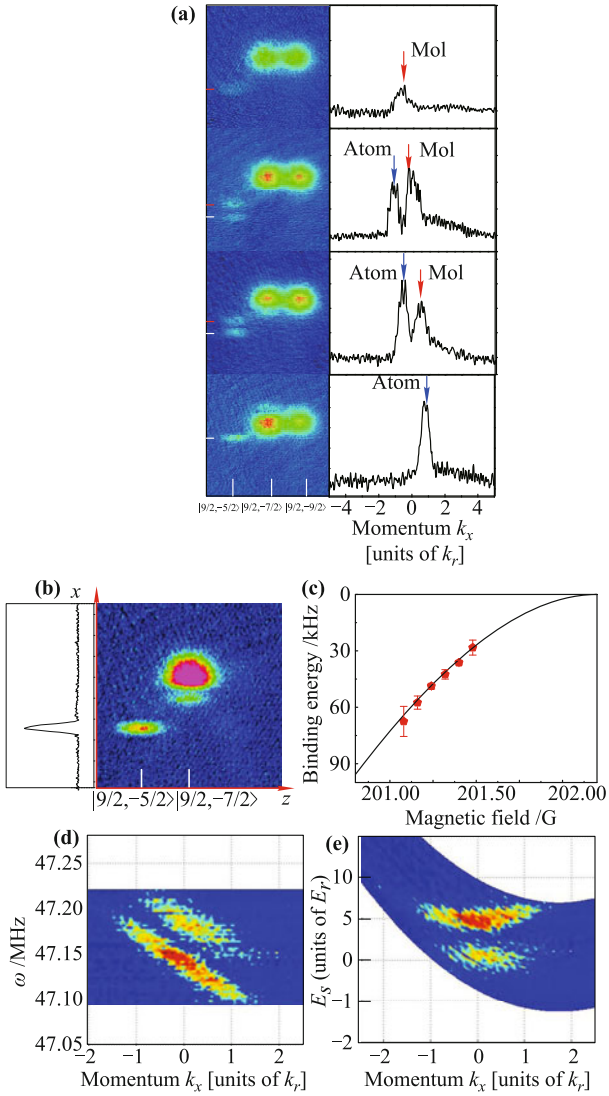


**Fig. 8** Raman spectroscopy of bound molecules and unpaired atoms in ultracold Fermi gas. **(a)** Absorption images of Fermi mixture and integrated optical density of atoms along $\pm\hat{z}$ direction in the $|9/2, -5/2\rangle$ state at 201.5 G with Raman frequency difference $\Delta\omega$ from 47.1 to 47.22 MHz. The short red (*white*) line in absorption images indicates the signal of molecule (unparired atoms). **(b)** Absorption images of Fermi gas and integrated optical density of atoms in $|9/2, -5/2\rangle$ state with the pure state $|9/2, -7/2\rangle$. **(c)** The measured binding energies (*red pentagon*) and theoretical values (*solid line*) of molecules on the BEC side of the s-wave Feshbach resonance are plotted versus magnetic fields. **(d)** The plot is an intensity map of the atoms in the $|9/2, -5/2\rangle$ state in the $(\Delta\omega, k_x)$ plane. The atomic density is displayed with the pseudo-color. The blue shaded regions correspond to the atomic density of zero. **(e)** The translated intensity spectrum shows the atomic number of unpaired atoms and bound molecules as a function of the single-particle energy (normalized to $E_r$ ) and momentum $k_x$ (normalized to $k_r$).

## 5 Conclusions and perspectives

In summary, we have investigated SO coupling for $^{87}$Rb BEC in the $F = 2$ hyperfine ground state by using two crossed 1064 nm optical dipole trap lasers to be the Raman beams. We considered three cases of loading the BEC into the Raman-dressed states by ramping the homogeneous bias magnetic field with three different paths. These artificial gauge potential also constitute novel tools to produce the synthetic magnetic or

electric field by means of a spatial or time dependence of the effective vector potential. We also explored the experimental realization of a SO coupled degenerate Fermi gas. The experiment realization of SO coupled BECs and degenerate Fermi gas is just beginning, it not only shed light on the outstanding problems of condensed matter physics such as Floquet topological insulators and Floquet Majorana fermions, but also yield completely new phenomena with no analogue elsewhere in physics. To simulate the true promise of these systems, it is better to engineer SO coupling that link spin to momentum in two and three dimensions in experiments, which is a central experimental task. Another unfortunate issue of light-induced SO coupling is the heating rates due to spontaneous emission in optical dipole potential and Raman coupling lasers. As we know, close to an optically allowed transition, one must contend with resonant absorption, which heats the gas. The crucial figure of merit is the ratio of the linewidth of the resonance to the fine structure splitting of excited state. This ratio is larger for lighter elements, which will therefore suffer more heating. For fermionic alkali atoms ($^6$Li and $^{40}$K) the heating rate is big problem because of the small fine-structure splitting of the P electronic levels compared to the transition linewidth. It may be a favorable choice to use a fermionic atom of the Lanthanide family, such as $^{167}$Er or $^{161}$Dy which benefit from narrow optical transitions.

We have demonstrated momentum-resolved Raman spectroscopy technology experimentally in the case of of ultracold Fermi gas on non-interacting regime and strongly interaction near an s-wave Feshbach resonance. In analogy to the angle-resolved photoemission spectroscopy of solid state physics, to probe the single particle property and measure the dispersion in an ultracold Fermi gas. We obtained the experiment results which are in good agreement with the expected quadratic dispersion. In the case of BEC side near an s-wave Feshbach resonances, we have shown a new measurement of the binding energy of molecules which is in good agreement with the calculation of the energy as a function of detuning from the resonance. The experimental results show many advantages of Raman spectrum compared to the RF and Bragg frequency technologies. Moreover there are still several significant advantages as compared to the RF spectroscopy, not shown in our experiment, but have been described in detail in theory[65]. This technology can be extended to the Fermi atom system to obtain the information on quasiparticle on the novel quantum states of matter, such as to probe the single particles properties with SO coupling in fermi gases, to study the quasiparticle state in BEC–BCS crossover, or under some effect of final state, especially its spacial selectivity is utilized.

**Acknowledgements** This work was supported by the National Basic Research Program of China (Grant No. 2011CB921601), the National Natural Science Foundation of China (NSFC, Grant No. 11234008), NSFC Project for Excellent Research Team (Grant No. 61121064), and Doctoral Program Foundation of the Ministry of Education China (Grant No. 20111401130001).

## References

1. W. Ketterle and M. W. Zwierlein, Making, probing and understanding ultracold Fermi gases, *Rivista del Nuovo Cimento*, 2008, 31: 247; arXiv: 0801.2500
2. C. Chin, R. Grimm, P. Julienne, and E. Tiesinga, Feshbach resonances in ultracold gases, *Rev. Mod. Phys.*, 2010, 82(2): 647
3. I. Bloch, J. Dalibard, and S. Nascimbène, Quantum simulations with ultracold quantum gases, *Nat. Phys.*, 2012, 8(4): 267
4. M. Greiner, O. Mandel, T. Esslinger, T. W. Hänsch, and I. Bloch, Quantum phase transition from a superfluid to a Mott insulator in a gas of ultracold atoms, *Nature*, 2002, 415(6867): 39
5. F. Jendrzejewski, A. Bernard, K. Müller, P. Cheinet, V. Josse, M. Piraud, L. Pezzé, L. Sanchez-Palencia, A. Aspect, and P. Bouyer, Three-dimensional localization of ultracold atoms in an optical disordered potential, *Nat. Phys.*, 2012, 8: 398
6. E. A. Donley, N. R. Claussen, S. L. Cornish, J. L. Roberts, E. A. Cornell, and C. E. Wieman, Dynamics of collapsing and exploding Bose–Einstein condensates, *Nature*, 2001, 412(6844): 295
7. E. A. Donley, N. R. Claussen, S. T. Thompson, and C. E. Wieman, Atom–molecule coherence in a Bose–Einstein condensate, *Nature*, 2002, 417(6888): 529
8. C. A. Regal, M. Greiner, and D. S. Jin, Observation of resonance condensation of fermionic atom pairs, *Phys. Rev. Lett.*, 2004, 92(4): 040403
9. T. Kraemer, M. Mark, P. Waldburger, J. G. Danzl, C. Chin, B. Engeser, A. D. Lange, K. Pilch, A. Jaakkola, H.-C. Nägerl, and R. Grimm, Evidence for Efimov quantum states in an ultracold gas of caesium atoms, *Nature*, 2006, 440(7082): 315
10. B. A. Bernevig, T. L. Hughes, and S. C. Zhang, Quantum spin Hall effect and topological phase transition in HgTe quantum wells, *Science*, 2006, 314(5806): 1757
11. M. König, S. Wiedmann, C. Brüne, A. Roth, H. Buhmann, L. W. Molenkamp, X. L. Qi, and S. C. Zhang, Quantum spin hall insulator state in HgTe quantum wells, *Science*, 2007, 318(5851): 766
12. K. W. Madison, F. Chevy, W. Wohlleben, and J. Dalibard, Vortex formation in a stirred Bose–Einstein condensate, *Phys. Rev. Lett.*, 2000, 84(5): 806
13. J. R. Abo-Shaeer, C. Raman, J. M. Vogels, and W. Ketterle, Observation of vortex lattices in Bose–Einstein condensates, *Science*, 2001, 292(5516): 476

14. E. Hodby, G. Hechenblaikner, S. A. Hopkins, O. M. Maragò, and C. J. Foot, Vortex nucleation in Bose–Einstein condensates in an oblate, purely magnetic potential, *Phys. Rev. Lett.*, 2002, 88(1): 010405
15. A. S. Sørensen, E. Demler, and M. D. Lukin, Fractional quantum Hall states of atoms in optical lattices, *Phys. Rev. Lett.*, 2005, 94(8): 086803
16. V. Schweikhard, I. Coddington, P. Engels, V. P. Mogendorff, and E. A. Cornell, Rapidly rotating Bose–Einstein condensates in and near the lowest Landau level, *Phys. Rev. Lett.*, 2004, 92(4): 040404
17. M. W. Zwierlein, J. R. Abo-Shaeer, A. Schirotzek, C. H. Schunck, and W. Ketterle, Vortices and superfluidity in a strongly interacting Fermi gas, *Nature*, 2005, 435(7045): 1047
18. Y. J. Lin, R. L. Compton, A. R. Perry, W. D. Phillips, J. V. Porto, and I. B. Spielman, Bose–Einstein condensate in a uniform light-induced vector potential, *Phys. Rev. Lett.*, 2009, 102(13): 130401
19. Y. J. Lin, R. L. Compton, K. Jiménez-García, J. V. Porto, and I. B. Spielman, Synthetic magnetic fields for ultracold neutral atoms, *Nature*, 2009, 462(7273): 628
20. Y. J. Lin, R. L. Compton, K. Jimnez-Garca, W. D. Phillips, J. V. Porto, and I. B. Spielman, A synthetic electric force acting on neutral atoms, *Nat. Phys.*, 2011, 7(7): 531
21. Y. J. Lin, K. Jiménez-García, and I. B. Spielman, Spin–orbit-coupled Bose-Einstein condensates, *Nature*, 2011, 471(7336): 83
22. Z. Fu, P. Wang, S. Chai, L. Huang, and J. Zhang, Bose–Einstein condensate in a light-induced vector gauge potential using 1064-nm optical-dipole-trap lasers, *Phys. Rev. A*, 2011, 84(4): 043609
23. J. Y. Zhang, S. C. Ji, Z. Chen, L. Zhang, Z. D. Du, B. Yan, G. S. Pan, B. Zhao, Y. J. Deng, H. Zhai, S. Chen, and J. W. Pan, Collective dipole oscillations of a spin-orbit coupled Bose–Einstein condensate, *Phys. Rev. Lett.*, 2012, 109(11): 115301
24. C. Qu, C. Hamner, M. Gong, C. Zhang, and P. Engels, Non-equilibrium spin dynamics and Zitterbewegung in quenched spin-orbit coupled Bose–Einstein condensates, arXiv: 1301.0658, 2013
25. M. Z. Hasan and C. L. Kane, Colloquium: Topological insulators, *Rev. Mod. Phys.*, 2010, 82(4): 3045
26. X. L. Qi and S. C. Zhang, Topological insulators and superconductors, *Rev. Mod. Phys.*, 2011, 83(4): 1057
27. P. Wang, Z. Q. Yu, Z. Fu, J. Miao, L. Huang, S. Chai, H. Zhai, and J. Zhang, Spin–orbit coupled degenerate Fermi gases, *Phys. Rev. Lett.*, 2012, 109(9): 095301
28. L. W. Cheuk, A. T. Sommer, Z. Hadzibabic, T. Yefsah, W. S. Bakr, and M. W. Zwierlein, Spin-injection spectroscopy of a spin–orbit coupled Fermi gas, *Phys. Rev. Lett.*, 2012, 109(9): 095302
29. M. Gong, S. Tewari, and C. W. Zhang, BCS-BEC crossover and topological phase transition in 3D spin–orbit coupled degenerate Fermi gases, *Phys. Rev. Lett.*, 2011, 107(19): 195303
30. Z. Q. Yu and H. Zhai, Spin–orbit coupled Fermi gases across a Feshbach resonance, *Phys. Rev. Lett.*, 2011, 107(19): 195305
31. L. Jiang, X. J. Liu, H. Hu, and H. Pu, Rashba spin–orbit-coupled atomic Fermi gases, *Phys. Rev. A*, 2011, 84(6): 063618
32. X. J. Liu, L. Jiang, H. Pu, and H. Hu, Probing Majorana fermions in spin–orbit-coupled atomic Fermi gases, *Phys. Rev. A*, 2012, 85(2): 021603
33. R. Liao, Y. X. Yu, and W. M. Liu, Tuning the tricritical point with spin–orbit coupling in polarized fermionic condensates, *Phys. Rev. Lett.*, 2012, 108(8): 080406
34. M. Gong, G. Chen, S. T. Jia, and C. W. Zhang, Searching for Majorana fermions in 2D spin–orbit coupled Fermi superfluids at finite temperature, *Phys. Rev. Lett.*, 2012, 109(10): 105302
35. H. Hu, H. Pu, J. Zhang, S. G. Peng, and X. J. Liu, Radio-frequency spectroscopy of weakly bound molecules in spin–orbit coupled atomic Fermi gases, arXiv: 1208.5841, 2012
36. Z. Zheng, M. Gong, Y. C. Zhang, X. B. Zou, C. W. Zhang, and G. Guo, Fulde–Ferrell–Larkin–Ovchinnikov phases in two-dimensional spin–orbit coupled degenerate Fermi gases, arXiv: 1212.6826, 2012
37. V. Galitski and I. B. Spielman, Spin–orbit coupling in quantum gases, *Nature*, 2013, 494(7435): 49
38. J. Radi, A. Di Ciolo, K. Sun, and V. Galitski, Exotic quantum spin models in spin–orbit-coupled Mott insulators, *Phys. Rev. Lett.*, 2012, 109(8): 085303
39. W. S. Cole, S. Zhang, A. Paramekanti, and N. Trivedi, Bose–Hubbard models with synthetic spin–orbit coupling: Mott insulators, spin textures, and superfluidity, *Phys. Rev. Lett.*, 2012, 109(8): 085302
40. Z. Cai, X. Zhou, and C. Wu, Magnetic phases of bosons with synthetic spin–orbit coupling in optical lattices, *Phys. Rev. A*, 2012, 85(6): 061605
41. D. Wei, D. Zh. Xiong, H. X. Chen, and J. Zhang, An enriched $^{40}$K source for atomic cooling, *Chin. Phys. Lett.*, 2007, 24: 679
42. D. Xiong, H. Chen, P. Wang, X. Yu, F. Gao, and J. Zhang, Quantum degenerate Fermi–Bose mixtures of $^{40}$K and $^{87}$Rb atoms in a quadrupole-Ioffe configuration trap, *Chin. Phys. Lett.*, 2008, 25: 843
43. P. Wang, H. Chen, D. Xiong, X. Yu, F. Gao, and J. Zhang, The design of quadrapole-Ioffe configuration trap for quantum degenerate Fermi–Bose mixtures, Acta. *Phys. Sin.*, 2008, 57(8): 4840 (in Chinese)
44. D. Xiong, P. Wang, Z. Fu, S. Chai, and J. Zhang, Evaporative cooling of $^{87}$Rb atoms into Bose–Einstein condensate in an optical dipole trap, *Chin. Opt. Lett.*, 2010, 8: 627 (in Chinese)
45. D. Xiong, P. Wang, Z. Fu, and J. Zhang, Transport of Bose–Einstein condensate in QUIC trap and separation of trapping spin states, *Opt. Express*, 2010, 18(2): 1649
46. I. B. Spielman, Raman processes and effective gauge potentials, *Phys. Rev. A*, 2009, 79(6): 063613

47. L. Zhang, J. Y. Zhang, S. C. Ji, Z. D. Du, H. Zhai, Y. J. Deng, S. Chen, P. Zhang, and J. W. Pan, Stability of excited dressed states with spin–orbit coupling, *Phys. Rev. A*, 2012, 87(1): 011601
48. X. J. Liu and H. Hu, Topological superfluid in one-dimensional spin–orbit-coupled atomic Fermi gases, *Phys. Rev. A*, 2012, 85(3): 033622
49. X. J. Liu, L. Jiang, H. Pu, and H. Hu, Probing Majorana fermions in spin–orbit-coupled atomic Fermi gases, *Phys. Rev. A*, 2012, 85(2): 021603
50. X. J. Liu, Zh. X. Liu, and M. Cheng, Manipulating topological edge spins in a one-dimensional optical lattice, *Phys. Rev. Lett.*, 2013, 110(7): 076401
51. L. Zhou, H. Pu, and W. Zhang, Anderson localization of cold atomic gases with effective spin–orbit interaction in a quasiperiodic optical lattice, *Phys. Rev. A*, 2013, 87(2): 023625
52. R. Wei and E. J. Mueller, Majorana fermions in one-dimensional spin–orbit-coupled Fermi gases, *Phys. Rev. A*, 2012, 86(6): 063604
53. P. Wang, Z. Fu, L. Huang, and J. Zhang, Momentum-resolved Raman spectroscopy of a noninteracting ultracold Fermi gas, *Phys. Rev. A*, 2012, 85(5): 053626
54. Z. Fu, P. Wang, L. Huang, Z. Meng, and J. Zhang, Momentum-resolved Raman spectroscopy of bound molecules in ultracold Fermi gas, *Phys. Rev. A*, 2012, 86(3): 033607
55. C. Chin, M. Bartenstein, A. Altmeyer, S. Riedl, S. Jochim, J. H. Denschlag, and R. Grimm, Observation of the pairing gap in a strongly interacting Fermi gas, *Science*, 2004, 305(5687): 1128
56. J. T. Stewart, J. P. Gaebler, and D. S. Jin, Using photoemission spectroscopy to probe a strongly interacting Fermi gas, *Nature*, 2008, 454(7205): 744
57. J. Simon, W. S. Bakr, R. Ma, M. E. Tai, P. M. Preiss, and M. Greiner, Quantum simulation of antiferromagnetic spin chains in an optical lattice, *Nature*, 2011, 472(7343): 307
58. E. Altman, E. Demler, and M. D. Lukin, Probing many-body states of ultracold atoms via noise correlations, *Phys. Rev. A*, 2004, 70(1): 013603
59. C. A. Regal and D. S. Jin, Measurement of positive and negative scattering lengths in a Fermi gas of atoms, *Phys. Rev. Lett.*, 2003, 90(23): 230404
60. S. Gupta, Z. Hadzibabic, M. W. Zwierlein, C. A. Stan, K. Dieckmann, C. H. Schunck, E. G. M. Van Kempen, B. J. Verhaar, and W. Ketterle, Radio-frequency spectroscopy of ultracold fermions, *Science*, 2003, 300(5626): 1723
61. Y. Shin, C. H. Schunck, A. Schirotzek, and W. Ketterle, Tomographic rf spectroscopy of a trapped Fermi gas at unitarity, *Phys. Rev. Lett.*, 2007, 99(9): 090403
62. Q. Chen and K. Levin, Momentum resolved radio frequency spectroscopy in trapped fermi gases, *Phys. Rev. Lett.*, 2009, 102(19): 190402
63. Q. Chen, Y. He, C. C. Chien, and K. Levin, Theory of radio frequency spectroscopy experiments in ultracold Fermi gases and their relation to photoemission in the cuprates, *Rep. Prog. Phys.*, 2009, 72: 122501
64. T. L. Dao, A. Georges, J. Dalibard, C. Salomon, and I. Carusotto, Measuring the one-particle excitations of ultracold fermionic atoms by stimulated Raman spectroscopy, *Phys. Rev. Lett.*, 2007, 98(24): 240402
65. T. L. Dao, I. Carusotto, and A. Georges, Probing quasiparticle states in strongly interacting atomic gases by momentum-resolved Raman photoemission spectroscopy, *Phys. Rev. A*, 2009, 80(2): 023627
66. G. Veeravalli, E. Kuhnle, P. Dyke, and C. J. Vale, Bragg spectroscopy of a strongly interacting Fermi gas, *Phys. Rev. Lett.*, 2008, 101(25): 250403
67. E. D. Kuhnle, S. Hoinka, P. Dyke, H. Hu, P. Hannaford, and C. J. Vale, Temperature dependence of the universal contact parameter in a unitary Fermi gas, *Phys. Rev. Lett.*, 2011, 106(17): 170402